Dalton Transactions

ROYAL SOCIETY OF CHEMISTRY

PAPER

View Article Online
View Journal | View Issue

Cite this: *Dalton Trans.*, 2026, **55**, 249

Mononuclear Fe^{II} and heterobinuclear $Fe^{II}Ni^{II}$ thiolate complexes derived from a compartmental hexaazadithiophenolato ligand: synthesis, structure and properties

Vanessa Stephan, Christian Zocher, Martin Börner, Jennifer Klose, Daniel Fuhrmann and Berthold Kersting *

Compartmental macrocycles have proven to be very successful for the synthesis of heterobinuclear transition metal complexes. We obtained a mixed-ligand FeNi thiolate complex, [FeNiL(μ-OAc)]ClO_4 (**3**), where L^{2-} represents a 24-membered hexaaza-dithiophenolato ligand, by metalation of either the mononuclear $[Fe^{II}(H_2L)](ClO_4)_2$ (**1**) or $[Ni^{II}(H_2L)](ClO_4)_2$ (**2**) complex with Ni^{II} or Fe^{II} salts in good to moderate yields. However, the homobinuclear $[Fe_2L(\mu\text{-OAc})]ClO_4$ (**4**), or $[Ni_2L(\mu\text{-OAc})]ClO_4$ (**5**), complexes are invariably formed as byproducts (≈12–15%). The metal atoms in **3** are bridged at a distance of 3.4588(5) Å by two thiolate residues and one external $\mu_{1,3}$-acetato ligand to give a bioctahedral $N_3Fe^{II}(\mu\text{-(SR)}_2(\mu\text{-OAc})Ni^{II}N_3)$ core structure. Magnetic susceptibility measurements for **3** show the presence of a *high-spin* Fe^{II} (S = 2) ion, which is antiferromagnetically coupled to the Ni^{II} (S = 1) ion to give a S_{total} = 1 ground state. Broken symmetry DFT calculations revealed J = −6.88 cm^{-1} ($H = -JS_1S_2$). The integrity and robust nature of complex **3** is maintained in solution as confirmed by ESI mass spectrometry and UV-vis-NIR spectroscopy. Cyclic voltammetry measurements for **3** in MeCN show two electrochemically quasi-reversible redox waves which are assigned to sequential oxidations of Fe^{II} and Ni^{II}, respectively ($E(Fe^{II/III})$ = +0.30 V, $E(Ni^{II/III})$ = +1.29 V *vs.* SCE). The $[Fe^{II}(H_2L)]^{2+}$ complex was isolated as a pale-yellow, paramagnetic (μ_{eff} = 5.41μ_B) perchlorate salt. It comprises a five-coordinated Fe^{II} ion in a distorted square-pyramidal N_3S_2 coordination environment, and a system of intramolecular N^+–H···S^- hydrogen bonds in the free pocket of the compartmental macrocycle.

Received 1st October 2025,
Accepted 19th November 2025

DOI: 10.1039/d5dt02350e

rsc.li/dalton

1. Introduction

In the past few decades, many heterobinuclear complexes have been investigated because of their specific chemical and physicochemical properties arising from the proximity of the two disparate metal centers.[1–3] Understanding the structural, electronic, and reactivity features of such complexes is of importance in the field of cooperative catalysis,[4–11] sensing, imaging,[12,13] and molecular magnetism.[14–16] Heterobinuclear complexes of first-row transition metal ions have also attracted much interest as structural mimics of the active site of certain metalloenzymes.[17–22] Compartmental macrocyclic ligands are popular for construction of heterobinuclear complexes due to their high binding selectivity and the macrocyclic effect that can lead to a higher thermodynamic stability of the complexes.[23–26] This is especially the case when combinations of labile 3d block metal ions are targeted.[27]

Heterobinuclear complexes derived from symmetrical phenol-based compartmental macrocycles have been known since the 1980s,[28,29] and their electrochemical and magnetic properties were extensively studied.[30–32] More recently, the catalytic activity of some heterobinuclear complexes has been reported.[33–38] Several synthetic procedures have been developed to access heterobinuclear complexes based on phenolate-containing macrocycles. In a comparably straightforward approach, the compartmental ligand can be generated *in situ* by templation with the desired metal-ions, M_1 and M_2 (Scheme 1, method 1). Accordingly, binuclear transition metal complexes are obtained, however, preferably of homobinuclear nature.[39] Thus, stepwise approaches aiming the complexation of one metal ion at the time are the better choice. Of great success for asymmetric complexes are pre-organized ligands which already coordinated one of the metal ions. Final cyclization then occurs *in situ* with complexation of the final M_2 (Scheme 1, method 2).[40] Furthermore, the exchange of labile

Institut für Anorganische Chemie und Kristallographie, Universität Leipzig, Johannisallee 29, 04103 Leipzig, Germany. E-mail: b.kersting@uni-leipzig.de; Fax: +49(0)341-97-36199

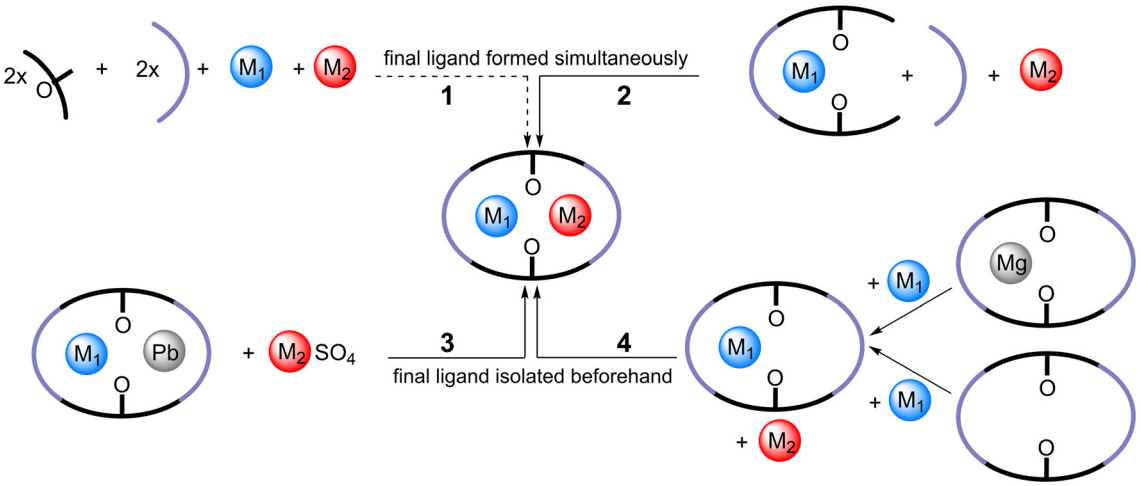

Scheme 1 Four approaches to generate heterobimetallic complexes supported by phenolate-based compartmental macrocycles. **1**: A 'one-pot' template-directed synthesis yields the compartmental complex. **2**: Final cyclization of pre-organized M_1 complex occurs along with insertion of M_2. **3**: Transmetallation of labile coordinated Pb^{II} ion accelerates insertion of M_2. **4**: Metal ions like Mg^{II} may aid the ligand synthesis by directed template condensation reaction or the ligand is available with free binding pockets. With the mononuclear M_1 complex, the second free binding pocket is available for M_2 insertion.

coordinated metal-ions in the second binding pocket, such as Pb^{II}, may be of advantage. The addition of M_2 sulfates leads to the precipitation of $PbSO_4$ and concomitant incorporation of M_2 (Scheme 1, method 3).[41–43] A particularly versatile approach targets the mononuclear M_1 complexes (Scheme 1, method 4), through metalation of the free ligand[44] or exchange with a templating agent like Mg^{II}.[45] In the final step, the second metal ion can easily be inserted.

Inspired by the abundance of catalytically active thiolate complexes in metalloenzymes and their synthetic models, we have synthesized and characterized several thiolato-bridged transition metal complexes supported by acyclic and macrocyclic polyaza–thiophenolato ligands.[46–48] A coordinatively-saturated $[Fe^{II}Ni^{II}L']^+$ complex supported by a compartmental N_6S_3 tripod ligand is a representative example (Fig. 1).[49] It should be noted that the above methods developed for phenolato-based macrocycles are of little synthetic value for the synthesis of such ligands. We have been successful by utilizing metal-free protocols using protected thioether precursor derivatives to access such ligands.

We have now been able to synthesize a bioctahedral FeNi complex with an active coordination site, namely [FeNiL(μ-OAc)]ClO_4 (**3**), by utilizing a related macrocyclic amino-thiophenolato ligand H_2L with an N_6S_2 donor set. The active coordination site in **3** is occupied by the acetato ligand. A stepwise approach comprising metalation reactions of mononuclear $Fe^{II}N_3S_2$ (or $Ni^{II}N_3S_2$) metalloligands (**1**, **2**) was devised to synthesize such a complex. The formation of intramolecular hydrogen bonds blocks one of the coordination sites allowing for the isolation of the mononuclear intermediate complexes **1** and **2**. Herein, we report on the synthesis, structure, and physicochemical properties of this new heterobinuclear $Fe^{II}Ni^{II}$ complex. The synthesis and characterization of the new

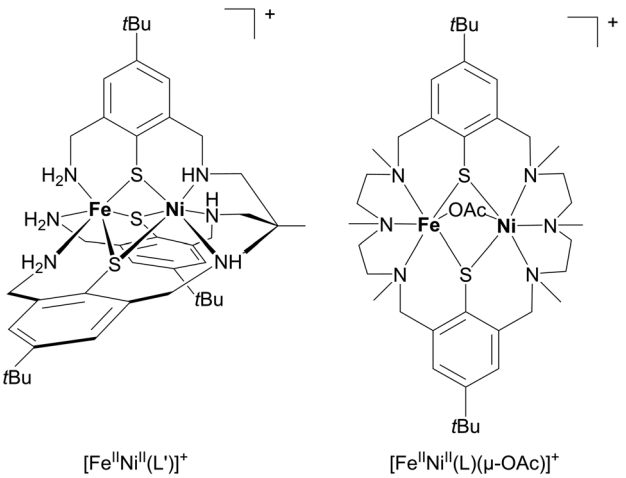

Fig. 1 Heterobinuclear $Fe^{II}Ni^{II}$ complexes supported by compartmental amino-thiophenolato ligands. The $[Fe^{II}Ni^{II}L']^+$ complex has been reported previously.[49]

complex $[Fe(H_2L)](ClO_4)_2$ (**1**) is also reported. To our knowledge, only few heterobinuclear FeNi complexes derived from macrocyclic ligands are reported in literature. The complex $[NiFeL]^{2+}$ supported by a $Py_2N_4S_2$ macrocycle is an example.[50]

2. Results and discussion

Syntheses of the complexes $[Fe(H_2L)](ClO_4)_2$ (1) and [FeNiL(μ-OAc)](ClO_4) (3)

The macrocyclic ligand H_2L is known to form mono- as well as binuclear complexes with various 3d block metal ions.[51,52] A mononuclear Fe^{II} complex has not been reported previously

and was considered as a precursor for a heterobinuclear $Fe^{II}Ni^{II}$ complex. Thusly, $Fe(ClO_4)_2{\cdot}6\ H_2O$, NEt_3, and $H_2L{\cdot}6HCl$ were reacted in a 1 : 6 : 1 stoichiometric ratio in MeOH under N_2 (Scheme 2) for 24 h to afford a pale-yellow solution, from which an off-white, air-sensitive, paramagnetic perchlorate salt of composition $[Fe(H_2L)](ClO_4)_2$ (**1**) was isolated in 69% yield. Once the Fe^{II} complex **1** was synthesized, its metalation with Ni^{II} salts was attempted. When a solution of $[Fe(H_2L)](ClO_4)_2$ **1** in MeOH/MeCN was treated with $Ni(OAc)_2{\cdot}4H_2O$ and NEt_3 as a base for 4 d at room temperature, a yellow solution formed, from which a golden-orange, paramagnetic, mixed-ligand $[Fe^{II}Ni^{II}L(\mu\text{-}OAc)]^+$ complex could be reproducibly isolated as a perchlorate salt (**3**) albeit in moderate yield (42%) and invariably contaminated by the known homobinuclear $[Fe_2L(\mu\text{-}OAc)]ClO_4$ (**4**) and $[Ni_2L(\mu\text{-}OAc)]ClO_4$ (**5**) complexes. The total amount of the byproducts was estimated to be ≈12% on the basis of a mass spectrometric analysis (see the SI). Complex **3** could also be obtained in good yield (80%) by reaction of the Ni^{II} complex **2** with anhydrous $Fe(OAc)_2$ and NEt_3 in MeOH/MeCN, but again contaminated with **4** and **5**. All attempts to separate **3** from **4** and **5** have failed so far.

We performed control experiments to examine whether metal scrambling occurs in the complex **3** in the solution state. Therefore, a 1 : 1 mixture of genuine samples of the homobinuclear complexes **4** and **5** was left to stir for several days at room temperature, as indicated in eqn (1). According to mass spectrometric analysis, the initial 1 : 1 ratio of the two complexes **4** and **5** remained unchanged. A similar experiment was conducted with complex **3**, which was contaminated with **4** and **5**. Again no changes in the stoichiometric composition could be detected after stirring for several days. The absence of metal scrambling was further confirmed by UV/vis spectroscopy and cyclic voltammetry (*vide infra*). It can be concluded that the integrity of complex **3** is maintained in solution state and that the byproducts **4** and **5** form during complexation reactions of the mononuclear species **1** and **2**.

$$\underset{\mathbf{4}}{[Fe^{II}{}_2L(\mu\text{-}OAc)]ClO_4} + \underset{\mathbf{5}}{[Ni^{II}{}_2L(\mu\text{-}OAc)]ClO_4} \xrightleftharpoons[\text{r.t.}]{\text{MeOH/MeCN}} 2\ \underset{\mathbf{3}}{[Fe^{II}Ni^{II}L(\mu\text{-}OAc)]ClO_4} \quad (1)$$

The two new compounds have been characterized by elemental analysis, mass spectrometry, UV-vis-NIR and FTIR spectroscopy, variable-temperature magnetic susceptibility measurements, cyclic voltammetry (for **3**), X-ray crystallography, X-ray powder diffraction (for **1**) and SEM-EDX (for **3′**). The synthesis and characterization of compounds **2**, **4**, and **5** has been reported previously.[53,54] As demonstrated in these earlier studies, the choice of counter-ion has a negligible effect on their spectroscopic and electronic properties. Therefore, unless otherwise noted, all compounds are discussed in their ClO_4^- salt form.

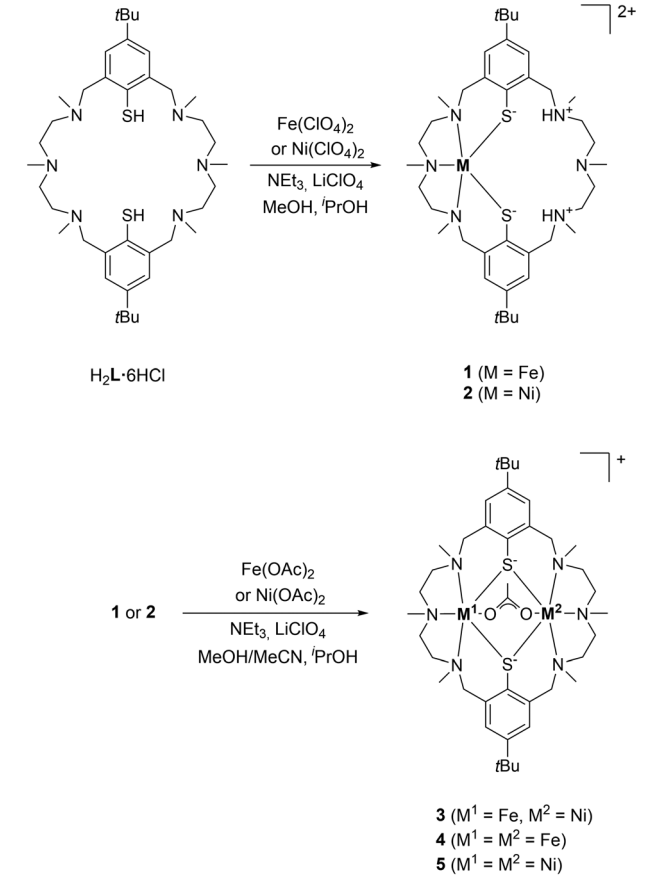

Scheme 2 Synthesis of complexes **1**–**5** as ClO_4 salts; salt metathesis to the BPh_4 salts yielded **3′**, **4′** and **5′**.

Crystallographic characterization of the complexes $[Fe(H_2L)](ClO_4)_2$ (1) and $[FeNiL(\mu\text{-}OAc)]BPh_4$ (3′)

Single-crystals of the perchlorate salt **1**·MeOH suitable for X-ray crystallographic analysis were obtained by slow diffusion of Et_2O into a concentrated MeOH solution. The title compound crystallizes in the monoclinic space group $P2_1/n$. The asymmetric unit contains one independent complex dication, two ClO_4^- anions, and one MeOH solvent molecule. Fig. 2 displays a perspective view of the molecular structure of the $[Fe(H_2L)]^{2+}$ dication, as well as a ball and stick model of the immediate coordination environment of the Fe atom. Selected bond lengths and angles are given in the Figure caption (see the SI for a full list of crystallographic and metrical data).

The Fe atom in **1** is five-coordinated by three nitrogen and two thiophenolato–sulphur atoms. The coordination sphere is best described as distorted square pyramidal, as manifested by the τ value of 0.36.[55] A similar value was found for the isostructural $[Ni(H_2L)](ClO_4)_2$ complex (**2**, τ = 0.29).[53] The average Fe–S and Fe–N bond lengths at 2.3401(8) Å and 2.241(2) Å, respectively, show no unusual features and match well with those of other five-coordinated FeN_3S_2 complexes.[56–58] For instance, in the distorted trigonal bipyramidal complex $[Fe^{II}S_2N_3(Pr,Pr)]$[56] ($S_2N_3(Pr,Pr)$ = 1,2-dimethyl-3,7,1-triazatridecane-1,13-dithiolate) the average Fe–S and Fe–N bonds are of length 2.353(1) and 2.177(6) Å.

The two hydrogen atoms bonded to N4 and N6 are involved in intramolecular hydrogen bonding interactions as illustrated

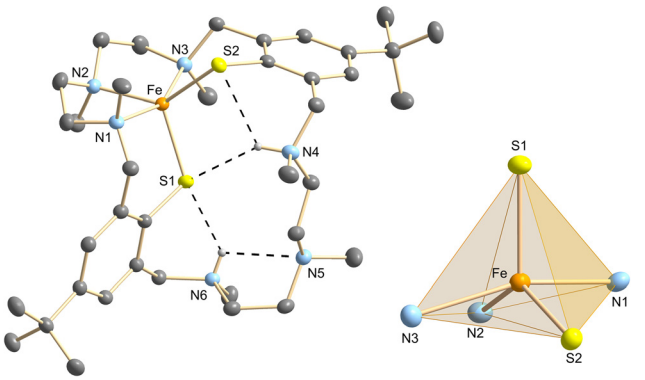

Fig. 2 Left: Ellipsoid representation of the molecular structure of the $[Fe^{II}(H_2L)]^{2+}$ dication in crystals of $[Fe(H_2L)](ClO_4)_2{\cdot}MeOH$ (**1**·MeOH) (CCDC 2392032). Thermal ellipsoids drawn at 30% probability level. Hydrogen atoms (except H4 and H6) were omitted for clarity. Dashed lines refer to intramolecular NH···S hydrogen bonding interactions. Right: The coordination polyhedron of the Fe atom in complex **1**. Selected interatomic distances and bond angles: N4···S1 3.777(2), N4···S2 3.230(2), N6···S1 3.111(1), N4···N6 5.420(3), N6···N5 2.874(3), Fe–S1 2.3291(6), Fe–S2 2.3511(6), Fe–N1 2.269(2), Fe–N2 2.150(2), Fe–N3 2.305(2) Å; N1–Fe–N3 157.29(6)°.

in Fig. 2. According to Bondi's van der Waals radii criterion (N···S ≤ 3.35 Å, N···N ≤ 3.10 Å),[59] one direct (N4···S2, 3.23 Å) and one three-centred, or bifurcated, hydrogen bond (N6···S1/N5, 3.11, 2.87 Å) are present. The latter involves two acceptor atoms – specifically, a sulphur and a nitrogen atom. Bifurcated hydrogen bonds are comparably rare. In the mixed ligand complex $[Ni(nmp)(S\text{-}o\text{-}babt)]^+$ (nmp = the deprotonated form of *N*-2 (mercaptoethyl)picolinamide, S-*o*-babt = thiolate of *o*-benzoylaminobenzene thiol) a bifurcated hydrogen bond is present, the corresponding N···S distances being 2.954 and 3.308 Å.[60]

In general, hydrogen bond donor acceptor distances, especially in bifurcated hydrogen bonds, can exceed the sum of van der Waals radii.[61] The presence (or absence) of such weak hydrogen bonding interactions may be more reliably determined by means of theoretical calculations.[62] Thus, we performed corresponding density functional theory (DFT) calculation at the B3LYP level of theory and the def2-SVP and def2-TZVP basis set followed by non-covalent interaction index (NCI) calculations,[63] in order to study the hydrogen bonding interactions in **1**. The NCI index determines the strength of the hydrogen bonds based on the associated electron density and its reduced density gradient.[63,64] Fig. 3 shows a representative NCI plot involving the two S and three N atoms in **1**. This plot clearly shows the presence of two bifurcated hydrogen bonds (N4···S1/S2 and N6···S1/N5). From the NCI fingerprint plot, the strength of the hydrogen bonds can be estimated.[65] Importantly, negative values correspond to attractive interactions with hydrogen bonds at higher density values ($-0.01 < p < -0.06$ au) and positive values show repulsive forces.[66,67] Therefore, the strongest interactions in **1** occur between N6–H···S1/N5 and N4–H···S2 with −0.027/−0.017 and −0.017 au respectively. The N6–H···N5 interaction is with

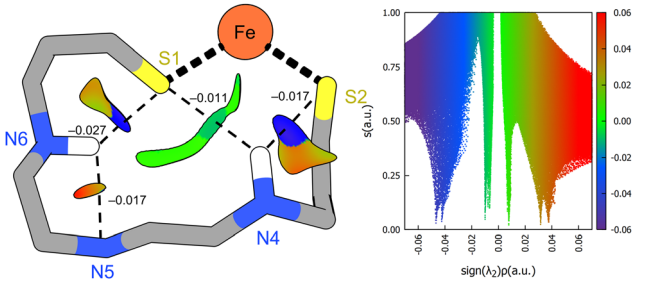

Fig. 3 NCI plot showing the presence of bifurcated N4···S1/S2 and N6···S1/N5 hydrogen-bonding interactions (dotted lines) in **1**. Gradient isosurfaces (s = 0.3 au) coloured on an RGB-inspired scale according to the sign(λ_2)ρ values over the range of −0.06 to 0.06 au. Blue surfaces indicate hydrogen bonds and green surfaces van der Waals interactions. Hydrogen atoms except those bound to N4 and N6 were omitted for clarity. Additional weak C–H···S1 hydrogen interactions are visible as smaller blue surfaces and not subject to further investigation.

−0.011 au the weakest. In contrast to the proposed hydrogen bonding based on the van der Waals radii criterion (N···S ≤ 3.35 Å, N···N ≤ 3.10 Å),[59] the NCI plot analysis supports the presence of two bifurcated hydrogen bonds instead of just one.

Single crystals of $[Fe^{II}Ni^{II}L(\mu\text{-}OAc)]BPh_4{\cdot}MeCN$ (**3′**·MeCN) suitable for X-ray crystallography were obtained by slow evaporation of a mixed MeCN/EtOH solution of **3** (contaminated by **4** and **5**) to which $NaBPh_4$ had been added. The structure comprises binuclear $[Fe^{II}Ni^{II}L(\mu\text{-}OAc)]^+$ complex (Fig. 4), BPh_4^- anions and MeCN solvate molecules. There is only one complex cation per asymmetric unit, with the Fe^{II} and Ni^{II} atoms statistically distributed (50 : 50) about the two metal binding sites. Thus, this crystal structure can only serve to confirm the atom connectivity of the $[Fe^{II}Ni^{II}L(\mu\text{-}OAc)]^+$ cation.

The $Fe^{II}Ni^{II}$ complex is isostructural with the corresponding Fe_2 (**4**) and Ni_2 complexes (**5**), with the metal atoms surrounded by three N and two S atoms from the macrocycle and one O atom from the bridging acetato ligand in a distorted octahedral fashion. The M···M distance in **3′** (3.4588(5) Å) is intermediate between that in **4′** (Fe···Fe 3.421(1) Å) and **5′** (Ni···Ni 3.483(1) Å), in agreement with the presence of two

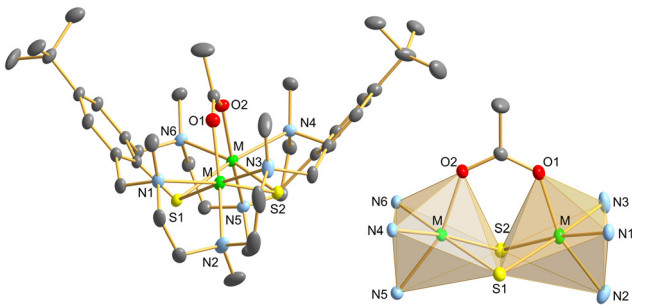

Fig. 4 Left: Molecular structure of the $[Fe^{II}Ni^{II}L(\mu\text{-}OAc)]^+$ cation in crystals of **3′**·MeCN (CCDC 2392031). Right: The coordination polyhedron of the metal ions. Thermal ellipsoids drawn at 30% probability level. All hydrogen atoms were omitted for clarity. The Fe and Ni atoms (M) are statistically distributed (50 : 50) about the two metal binding sites.

metal ions with different ionic radii (Fe^{II} 0.83, Ni^{II} 0.92 Å).[68,69] The same applies to the corresponding M–S and M–N distances. The long metal–ligand bonds in **3′** are indicative of a *high-spin* configuration for the Fe^{II} ion. Relative to the five-coordinated Fe^{II} in **1**, the average metal–S and metal–N distances in **3′** increase by 0.16 and 0.03 Å, respectively (see SI). To assess the distribution of Fe^{II} and Ni^{II} within a single crystal as well as among a mixture of crystals, SEM–EDX analyses were carried out with **3′**·MeCN. The measurements indicate a largely homogeneous elemental distribution (see SI).

Spectroscopic characterization

FTIR spectroscopic measurements were carried out on complex **1** to probe potential N–H···S hydrogen bonding. However, for reasons unclear, no NH stretching bands could be detected in the characteristic range (3400–2500 cm^{-1}). Similar behavior was already noted for the isostructural $[Ni(H_2L)](ClO_4)_2$ (**2**) and $[Zn(H_2L)](ClO_4)_2$ (**6**) complexes. So, the presence of these NH···S bonds relies solely on the basis of the distance criteria for NH···S bonding and the DFT calculations. The FTIR spectrum (Fig. S5) of **3** reveals two characteristic vibrations at 1592 and 1425 cm^{-1} attributed to the symmetric and asymmetric carboxylate stretches. The separation of the two modes is large ($\tilde{\nu}_{asym} - \tilde{\nu}_{sym}$ = 167 cm^{-1}) and consistent with a $\mu_{1,3}$-bridging acetato group as in **4** and **5**. The IR spectra of **3**, **4**, and **5** can be superimposed on one another. The three complexes could not be clearly resolved with the available spectral resolution.

The electronic absorption spectrum of complex **1**, recorded in MeCN solution, is presented in Fig. 5, with the corresponding data compiled in Table 1 alongside those of the isostructural Ni^{II} and Zn^{II} complexes **2** and **6**. Since complex **6** does not exhibit charge-transfer or d–d transitions, its spectral profile is dominated by two intense π–π* absorptions in the UV region, both with extinction coefficients above 15 000 M^{-1} cm^{-1}, and a shoulder ≈313 nm. On this basis, the analogous features observed for complex **1** are likewise assigned to π–π* transitions. Additional shoulders around 298 and 328 cm^{-1} are discernible for complex **1**, which are tentatively attributed to ligand-to-metal charge transfer (LMCT). Comparable LMCT transitions of similar energy have previously been described for related five-coordinate Fe^{II} aryloxide complexes[70] and are also observed for **2**. The spectrum further reveals a weak d–d transition at ≈800 nm with an extinction coefficient below 50 M^{-1} cm^{-1}. A second d–d transition is expected above 2000 nm, which could not be detected with our experimental setup. The (two) d–d transitions are assigned to the $B_1(d_{x^2-y^2})$ and $A_1(d_{z^2})$ states (in pure, square-pyramidal (C_{4v}) geometry) as observed for other five-coordinated Fe^{II} complexes with the normal, doubly occupied d_{xy} ground state ($(d_{xy})^2(d_{xz})^1(d_{yz})^1(d_{z^2})^1(d_{x^2-y^2})^1$).[71–74]

Table 1 Electronic absorption spectral data for **1** (λ_{max}/nm; ε/M^{-1} cm^{-1}). The data for **2** and **6** are included for comparison

	$[Fe^{II}(H_2L)](ClO_4)_2$ (**1**)	$[Ni^{II}(H_2L)](ClO_4)_2$ (**2**)	$[Zn^{II}(H_2L)](ClO_4)_2$ (**6**)
π–π*	208(37 400), 266(18 800)	209(35 200), 250 (sh), 280(14 900)	211(34 500), 266 (25 700), 306(sh)
LMCT	298(10 500), 328(sh)	343(sh), 425 (900), 504(1200)	—
d–d transitions	806(33)	684(66)	—

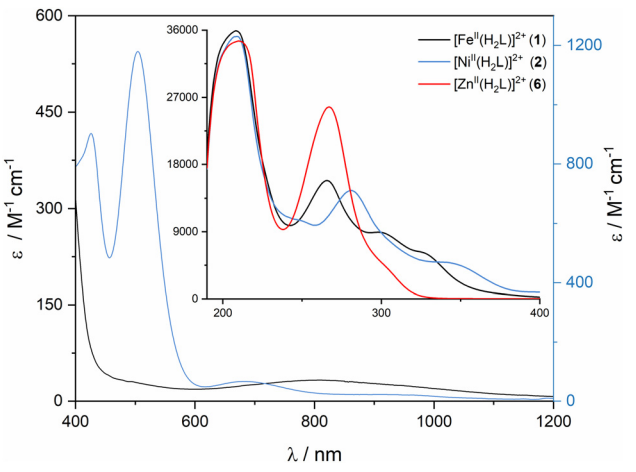

Fig. 5 Electronic absorption spectrum of the mononuclear Fe^{II} (**1**) complex in black (400–1200 nm, $c = 10^{-3}$ M, MeCN, 295 K). The inset shows the UV region 190–400 nm ($c = 10^{-5}$ M, MeCN, 295 K); spectra of **2** and **6** are shown for comparison.

Fig. 6 displays the electronic absorption spectrum of the $Fe^{II}Ni^{II}$ complex **3** in the vis-NIR region (600–1400 nm). The spectra of the homobinuclear complexes **4** and **5** are shown for comparison. The spectrum of **3** differs significantly from those of **4** and **5**, as one might expect for a heterobinuclear $Fe^{II}Ni^{II}$ species. This is particularly evident from the position and intensity of the characteristic d–d transition (ν_2, $^3T_{1g} \leftarrow {}^3A_{2g}$ designation in pure O_h symmetry) for the six- coordinated Ni^{II} (d^8, $S = 1$) ion. This transition is significantly red-shifted from 648 in **5** to 660 nm in **3**. Likewise, the extinction coefficient decreases from 28 to 17 M^{-1} cm^{-1}. For a 50%/50% mixture of **4** and **5** no red-shift would be expected. Two further weak absorptions at λ_{max} = 907 (shoulder) and 1188 nm are clearly discernible in the NIR region for complex **3**. A deconvolution analysis of the spectrum reveals three ligand-field based transitions for six-coordinated Fe^{II} ions (885 and 1275 nm) and Ni^{II} (1164 nm) ions, as illustrated in Fig. 6. The former transitions can be assigned to the components of the $^5E \leftarrow {}^5T_2$ absorption of a *high-spin* Fe^{II} (d^6, $S = 2$) ion, split by a dynamic Jahn–Teller effect in the excited ^5E state which is typical for *high-spin* Fe^{II} compounds.[75] The remaining absorption at 1164 nm is then readily assigned to the ν_1 ($^3T_{2g}(F) \leftarrow {}^3A_{2g}$) ligand field transition of a six-coordinated Ni^{II} ($S = 1$) ion. Again, these values are different from those seen for the homobinuclear complexes (937(14), 1239(36) for **4**, 1134(55) for **5**).[54,76] The third d–d transition of the Ni^{2+} ion, ν_3 expected at ≈400 nm, is obscured by intense bands arising from thiolate-to-M^{2+} charge transfer transitions (λ_{max} = 395 nm, ε = 2640

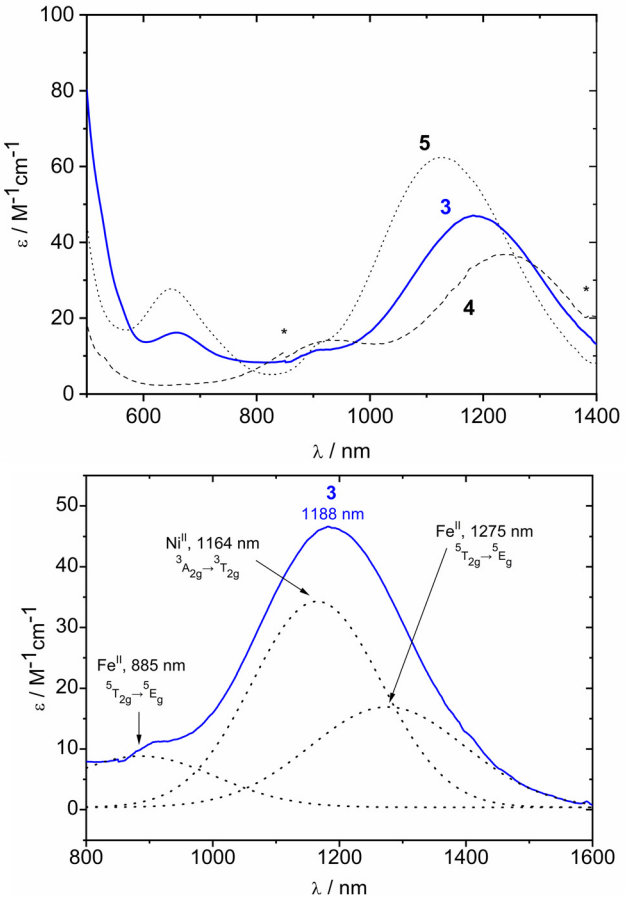

Fig. 6 Top: vis-NIR spectra for complexes **3–5** in MeCN ($c \approx 10^{-3}$ M, 295 K). The absorption marked with an asterisk is related to the spectrometer. Bottom: Deconvolution of the absorptions of **3** in the 800–1600 nm range.

M^{-1} cm^{-1}).[77] Overall, the electronic absorption spectrum suggests that complex **3** exists as a stable heterobinuclear $Fe^{II}Ni^{II}$ complex comprising a six-coordinated *high-spin* Fe^{II} (S = 2) and a six-coordinated Ni^{II} (S = 1) ion. The ligand field strength in the N_3S_2O compartment is thus surprisingly low, comparable to a ligand field produced by six oxygen (aqua) donors. This is in contrast to the complex $[Fe^{II}Ni^{II}L']^+$ which comprises a *low-spin* Fe^{II} centre.[49]

Variable temperature magnetic susceptibility measurements

In order to confirm oxidation and spin states, variable temperature magnetic susceptibility measurements were carried out in an applied magnetic field of 0.05 T over a temperature range of 2–300 K for complex **1** and of 0.5 T for complex **3**. Fig. 7 shows the effective magnetic moment μ_{eff} (per mononuclear Fe^{II} complex **1**) *versus* T.

The effective magnetic moment at room temperature of 5.41μ_B decreases steadily to 60 K (5.27μ_B) and then rapidly to 4.44μ_B at 2 K, which may be due to zero-field splitting effects and intermolecular exchange interactions. Nevertheless, the room temperature value is clearly comparable to other five-coordinated *high-spin* Fe^{II} (d^6, S = 2) complexes with μ_{eff} being close to the spin-only value of 4.90μ_B.[78,79] Fig. 8 shows the temperature dependence of the effective magnetic moment μ_{eff} (per binuclear complex) for the (impure) $Fe^{II}Ni^{II}$ complex **3**. The data for complexes **4** and **5** are displayed for comparison.[54] The susceptibility data of complex **3** was recorded for a powdered sample between 2 and 300 K in an applied external magnetic field of B = 0.5 T. The effective magnetic moment at room temperature (6.30μ_B) is much higher than expected for two non-interacting *high-spin* Fe^{II} (d^6, S = 2) and Ni^{II} (d^8, S = 1) ions with g = 2.0 (5.66μ_B). With decreasing temperature, the magnetic moment decreases steadily to 1.83μ_B at 2 K. This behavior is indicative of a weak antiferromagnetic superexchange

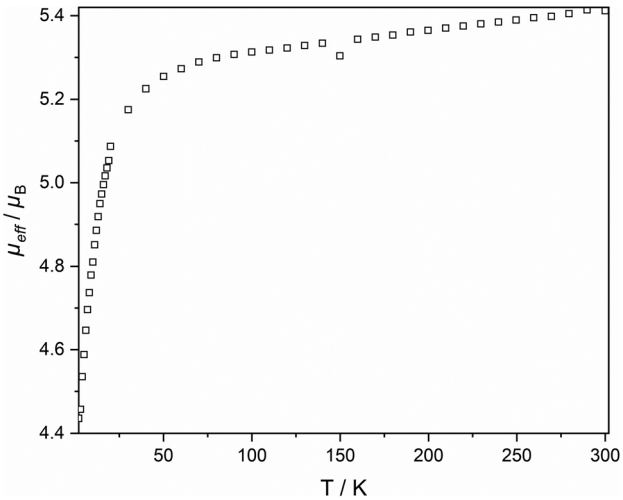

Fig. 7 Temperature dependence of the μ_{eff} value for the mononuclear complex **1** at 0.05 T.

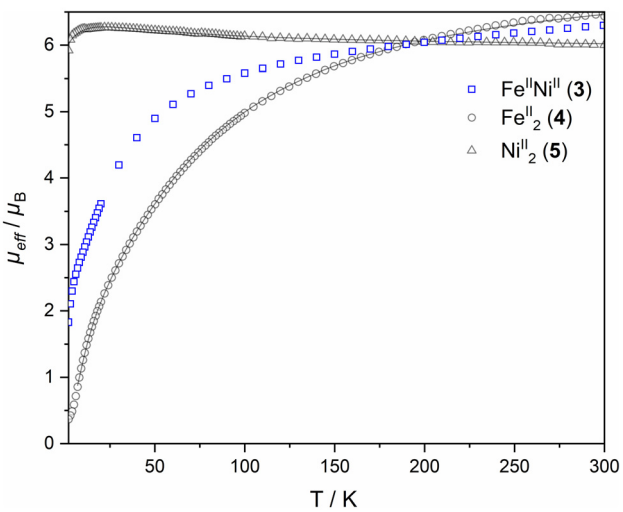

Fig. 8 Blue curve: measured temperature dependence of the effective magnetic moment μ_{eff} (at 0.5 T) for **3**. Due to contaminations, a fit of the data was omitted. Black curves: the effective magnetic moments μ_{eff} (at 0.2 T) for **4** and **5** with solid lines corresponding to the best fit.[54]

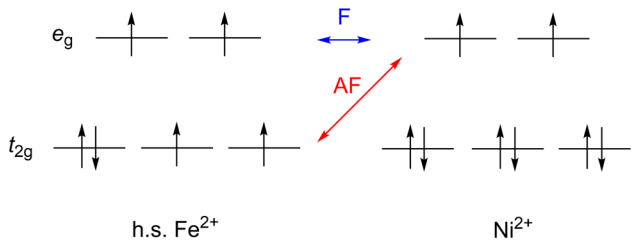

Fig. 9 Exchange interactions by ferromagnetic (F) or antiferromagnetic (AF) coupling for the $Fe^{II}Ni^{II}$ complex.

interaction. However, the expected maximum in the χ_m *vs.* T plot (SI) is not observed at low temperatures. This can be traced to the small amounts of the paramagnetic impurities **4** and **5** in the sample.

Due to the homobinuclear impurities, no reasonable fits of the magnetic susceptibility data could be obtained for complex **3**. Consequently, broken symmetry DFT calculations (PBE0/def2-TZVP level of theory) were performed. These calculations confirmed an antiferromagnetic exchange interaction. The exchange coupling parameter $J = -6.88$ cm^{-1} ($H = -JS_1S_2$) was calculated.[80] The antiferromagnetic exchange interaction in **3** is somewhat weaker than in the Fe^{II} complex **4** ($J = -11.97$ (DFT), -10.63 (experiment)[54] cm^{-1}). This may be traced to the decrease of exchange interactions of the $t_{2g} \leftrightarrow e_g$ type (expected to be antiferromagnetic in nature) although other effects cannot be ruled out.[81a] To gain deeper insight into the pathways mediating the interaction between the paramagnetic Fe^{II} and Ni^{II} sites, we examined the direct and differential overlap of the corresponding orbital pairs obtained from the Broken symmetry density functional theory solutions for **3**, as done for other triply bridged Cr^{III} complexes.[81b,c] The results of the corresponding orbital transformations are shown in Fig. S9. The small overlap integrals for the corresponding orbital pairs (0.063, 0.042 for the orbitals 222, and 223, respectively), suggest that direct metal–metal through-space interactions are not significant in the present complex.

The BS-DFT calculations further reveals that the two magnetic orbitals in **3** resemble the Fe^{II} d_{xz} and d_{yz} orbitals as well as the Ni^{II} d_{z^2} and $d_{x^2-y^2}$ orbitals. In the case of these orbital pairs, overlap occurs over the bridging ligands.[81b] BS-DFT calculations on truncated model complex **3″** (with the carboxylate bridge removed) have also been performed to study the individual contributions of the carboxylate ligands and thiolato bridges to the overall magnetic behaviour. This approach has previously proven to be a powerful tool to unravel the contributions of the individual bridges in Ni complexes supported by $(L)^{2-}$.[81b,c] The results imply that a dominant "antiferromagnetic" contribution (-17.11 cm^{-1} (**3″**) Table S8) through the bridging thiolates is counterbalanced by a ferromagnetic interaction by the carboxylato bridge (Fig. 9).

Cyclic voltammetry

Despite small impurities, the distinctive properties of complex **3** can still be evaluated by means of cyclovoltammetry. The

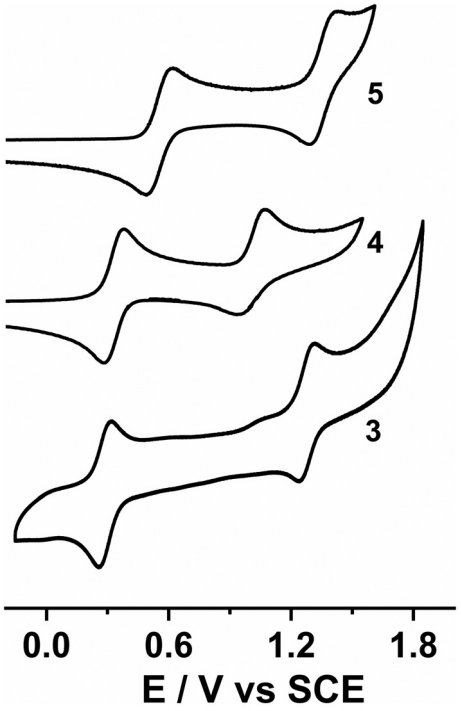

Fig. 10 Cyclic voltammograms for **3–5** in MeCN (10^{-3} M, 0.1 M nBu$_4$PF$_6$), Pt-disk working electrode, Pt-wire counter electrode, Ag wire reference electrode, scan rate = 100 mV s^{-1}.

cyclic voltammogram (CV) recorded in MeCN containing 0.1 M nBu$_4$NPF$_6$ as the supporting electrolyte at 298 K shows two electrochemically quasi-reversible redox waves at $E_{1/2} = +0.30$ V *vs.* SCE ($\Delta E_p = 90$ mV) and at +1.29 V ($\Delta E_p = 93$ mV), respectively. The CV of **3** clearly differs from those of **4** and **5**. The two redox waves can be assigned to sequential one-electron oxidations to the formal $Fe^{III}Ni^{II}$ and $Fe^{III}Ni^{III}$ redox states, respectively, by comparison with the CVs of **4** and **5** (Fig. 10). Not many redox-active $Fe^{II}Ni^{II}$ thiolate complexes have been reported.[82,83] The $[FeNiL']^+$ complex supported by the tripodal N_6S_3 ligand,[49] is oxidized at much more cathodic potentials (-0.43 V, +0.45 V *vs.* SCE). The shifts of +0.73 V and +0.84 V for the two oxidations of **3** relative to those in $[FeNiL']^+$ are consistent with the much weaker ligand field in **3**. Stronger donors in $[FeNiL']^+$ that lie on the right-hand side in the spectrochemical series (primary and secondary amine) are replaced by weak field donors in **3** that are further to the left (tertiary amine, carboxylate) to destabilize the divalent oxidation states, thereby causing the shifts in the redox potential.

3. Conclusion

Several synthetic routes for preparing heterobinuclear complexes have been developed. Considerable success has been achieved in case of NiFe complexes using the *cis*-thiolate strategy, with significant contributions reported by Darensbourg *et al.* (Scheme 3, common approach 1). The approach relies on

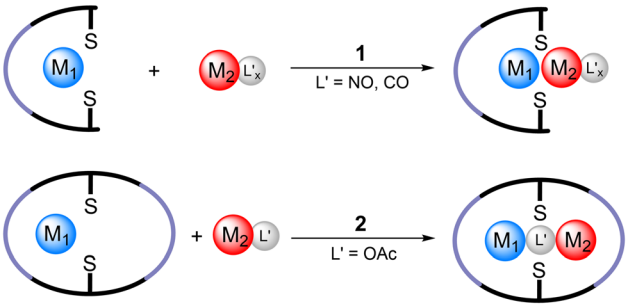

Scheme 3 Comparison of approaches to generate heterobimetallic complexes supported by thiophenolato-based ligands; **1**. the approach by Darensbourg *et al.* based on the reaction of a $M_1N_2S_2$ synthon with $M_2(CO)_x$ or $M_2(NO)_x$ fragments; **2**. the stepwise strategy utilizing macrocyclic compartments presented herein.

coupling pre-formed MN_2S_2 metallodithiolato synthons with reactive $M(CO)_x$ or $M(NO)_x$ units, allowing both structural variability and the formation of various heterobimetallic FeNi complexes. This approach does not lead to homobinuclear byproducts.[19]

A newly prepared mononuclear Fe^{II} complex with a N_3S_2 coordination sphere is presented and fully characterized by UV-vis-NIR and ATR-FTIR spectroscopy, single crystal X-ray crystallography, and SQUID magnetometry. Additionally, the complex exhibits advantageous N^+–H···S^- hydrogen bonding, which facilitates the synthesis of heterobinuclear complexes. The presence of this interaction was confirmed through NCI plot analysis.

The main findings of this paper are as follows: an air-stable heterobimetallic $Fe^{II}Ni^{II}$ complex featuring an active coordination site was successfully synthesized using a macrocyclic N_6S_2 ligand. While the isolated product contained a minor proportion (≈12–15%) of homobinuclear complexes **4** and **5**, its preparation nonetheless demonstrates the feasibility of forming the desired heterometallic species. Because the intermediate mononuclear and homobinuclear complexes were independently obtained and fully characterized in pure form, the properties of the target heterobinuclear complex could be evaluated in a comprehensive and well-supported manner.

In the molecular crystal structure of the heterobinuclear complex, **3′**, the metal ions are bridged by an acetate group with a M–M distance of 3.4588(5) Å, which is intermediate of the Fe–Fe and Ni–Ni distances in the homobinuclear complexes **4′** and **5′**. The UV-vis-NIR spectra differ significantly from those in the homobinculear species which speaks in favour of a heterobimetallic complex, instead of a 50/50% mixture of the homobinuclear complexes. This is further supported by magnetic susceptibility measurements which imply antiferromagnetic coupling of a *high spin* Fe^{II} ($S = 2$) with Ni^{II} ($S = 1$) to produce an overall $S_{total} = 1$. The coupling constant of $J = -6.88$ cm^{-1} ($H = -JS_1S_2$) was determined by DFT calculations. Finally, the redox potential of $Fe^{II/III}$ is with +0.30 V much lower than that of $Ni^{II/III}$ with 1.29 V *vs.* SCE in MeCN.

Future advances target the issue of metal scrambling. Separation of the hetero- from the homobinuclear complexes may be realized by either exploiting the different redox potentials of complex **3**, **4** and **5** or take advantage of different chemical reactivity. Alternatively, the formation of homobinuclear complexes may be impeded by utilizing the corresponding deprotonated complex of compounds **1** or **2** for better integration of the second metal ion.

Of major interest is the binding mode of the coordination site in complex **3**. For instance, exchanging the acetato ligand with a hydride ion could ease the understanding of functionality in several enzymes.[17–22]

4. Experimental

Materials and methods

All reagents were purchased from commercial sources unless otherwise specified. Anhydrous methanol was prepared by refluxing over magnesium, distilled and stored over N_2. Mass spectra were recorded with ESI(+) ionization on a Bruker Daltronics Esquire 3000 Plus ITMS or Impact II UHR Qq-TOF instrument. Isotope patterns were simulated using MestReNova 11.0, the estimation of contamination with homobinuclear species was established by systems of linear equations. Infrared spectra (4000–400 cm^{-1}) were recorded at 2 cm^{-1} resolution and measured with 32 scans on a Bruker-Vertex 80 V FTIR spectrometer using a diamond-ATR unit or the Bruker Tensor 27 spectrometer. Spectra of complexes **1** and **3** were collected at room temperature on a Jasco V-670 UV-vis-NIR spectrophotometer, equipped with a photomultiplier and a PbS photoconductive cell. The spectrum was collected in the 190–1600 nm range with a resolution of 2 nm.

Caution! Perchlorate salts of transition-metal complexes are hazardous and may explode. Only small quantities should be prepared and great care should be taken.

$[Fe(H_2L)](ClO_4)_2$ (1). To a solution of $Fe(ClO_4)_2{\cdot}6\ H_2O$ (60 mg, 0.17 mmol, 0.95 eq.) and $H_2L{\cdot}6$ HCl (156 mg, 0.18 mmol, 1 eq.) in anhydrous MeOH (50 mL) was added a 1 M solution of NEt_3 in MeOH (1.05 mL, 1.05 mmol, 6 eq.) was added. The solution turned pale yellow. The reaction was stirred for 1 d. Then, a solution of $LiClO_4{\cdot}3H_2O$ (281 mg, 1.7 mmol, 10 eq.) in ^{i}PrOH (10 mL) was added. The mixture was concentrated under reduced pressure to give a white solid, which was filtered, washed with cold ^{i}PrOH and dried in vacuum. Further purification was done by slow diffusion of Et_2O into a concentrated MeOH solution, to obtain a fine crystalline product. Yield: 112 mg (69%), off-white powder. UV/Vis (CH_3CN): λ_{max} (ε) = 208 (37 355), 266 (18 743), 298 (10 501), 328 (sh), 806 (33) nm. IR (KBr, 22°) = 2962 (m), 2913 (m), 2905 (m), 2869 (m), 1630 (w), 1466 (s), 1365 (w), 1301 (w), 1230 (w), 1153 (m), 11 212 (s), 1108 (s), 1096 (s), 1014 (w), 890 (w), 844 (w), 819 (w), 636 (w), 624 (s) cm^{-1}. ESI-MS (MeCN): *m*/*z* 363.19 [M–$2ClO_4$]$^{2+}$, 725.38 [M–H–$2ClO_4$]$^+$, 825.33 [M–ClO_4]$^+$. Elemental analysis calc (%) for $C_{39}H_{72}Cl_2FeN_6O_{10}S_2$ (**1**·MeOH·H_2O, 974.35): C 48.00, H 7.44, N 8.61; found: C 48.03, H 7.34, N 8.02. Based on the PXRD data recorded for **1**·MeOH, the compound can be identified as phase-pure with respect to crystalli-

nity with an amorphous component due to sample preparation. Further details are provided in the SI.

[FeNiL(μ-OAc)]ClO_4 (3). Method A: A solution of $[Fe(H_2L)](ClO_4)_2$ (67 mg, 0.072 mmol, 1.00 eq.), $Ni(OAc)_2{\cdot}4H_2O$ (18 mg, 0.72 mmol, 1.00 eq.), and NEt_3 (15 μL, 0.14 mmol, 2 eq.) in MeOH/MeCN (40 mL (1 : 1)) was stirred for 4 d. Then, a solution of $LiClO_4{\cdot}3H_2O$ (58 mg, 0.861 mmol, 5 eq.) in ^{i}PrOH (5 mL) was added. The mixture was concentrated under reduced pressure to give an orange-brown solid, which was filtered, washed with cold ^{i}PrOH and dried in vacuum. The crude product was purified by recrystallization from MeCN/EtOH. Yield: 29 mg (42%), brown-orange, microcrystalline solid. UV/Vis (CH_3CN): λ_{max} ($\log \varepsilon$) = 193 (4.76), 308 (4.15), 476 (sh), 659 (1.20), 910 (sh), 1184 (1.67) nm. IR (KBr): $\tilde{\nu}$ = 3441 (br, w), 3022 (w), 2956 (m), 2905 (m), 2867 (m), 1630 (w), 1584 (s), 1552 (w), 1464 (s), 1424 (s), 1394 (w), 1367 (w), 1343 (w), 1302 (w), 1278 (w), 1228 (m), 1094 (br, s), 1016 (m), 971 (w), 929 (w), 911 (w), 896 (m), 852 (w), 819 (w), 792 (w), 759 (w), 742 (w), 656 (w), 624 (s), 599 (w), 537 (w), 478 (w), 455 (w) cm^{-1}. ESI-MS (MeCN): m/z 841.35 $[M–ClO_4]^+$. Elemental analysis calc (%) for $C_{40}H_{71}ClFeN_6NiO_8S_2$ (**3**·2H_2O, 978.15): C 49.12, H 7.32, N 8.59; found: C 49.58, H 6.94, N 8.63. Byproducts of $[Fe_2L(\mu\text{-}OAc)]ClO_4$ (**4**) and $[Ni_2L(\mu\text{-}OAc)]ClO_4$ (**5**) were determined with 12.5% by mass spectrometry.

Method B: A solution of $[Ni(H_2L)](ClO_4)_2$ (**2**) (100 mg, 0.11 mmol, 1 eq.), $Fe(OAc)_2$ (23 mg, 0.13 mmol, 1.2 eq.), and NEt_3 (31 μL, 0.22 mmol, 2 eq.) in MeOH (30 mL) was stirred for 3 d. Then a solution $LiClO_4{\cdot}3H_2O$ (35 mg 0.22 mmol, 2 eq.) in EtOH (25 mL) was added. The solvent was concentrated under reduced pressure to give an orange-brown solid, which was filtered, washed with cold EtOH and dried in vacuum. The crude product was purified by recrystallization from MeCN/EtOH. Yield: 81 mg (80%), orange-brown, microcrystalline solid. The analytical data for this material is identical with that prepared by method A. Byproducts of $[Fe_2L(\mu\text{-}OAc)]ClO_4$ (**4**) and $[Ni_2L(\mu\text{-}OAc)]ClO_4$ (**5**) were determined with 15.7% by mass spectrometry.

Magnetic measurements

The magnetic susceptibility measurements were performed with a MPMS 7XL SQUID magnetometer (quantum design). Respective data were collected in the temperature range of 2 to 300 K for an applied dc field of 0.05 T for complex **1** and of 0.5 T for complex **3**. The polycrystalline samples were grounded and were prepared in a gelatine capsule. The measured susceptibility data were corrected for the underlying diamagnetism, which was estimated using Pascal constants. The data were processed with the DAVE.[84]

Cyclic voltammetry

Cyclic voltammetry measurements were carried out at room temperature with an Autolab PGSTAT12 potentiostat/galvanostat. The cell contained a Pt disk working electrode, a Pt wire auxiliary electrode, and a Ag wire as reference electrode. Concentrations of sample solutions were 10^{-3} M in a 0.1 M supporting electrolyte (tetrabutylammonium hexafluorophosphate in MeCN). The scan rate was 100 mV s^{-1}. Ferrocene was used as internal standard. All potentials were converted to the SCE reference using tabulated values.[85]

X-ray crystallography

Suitable single crystals of $[Fe(H_2L)](ClO_4)_2{\cdot}$MeOH (**1**·MeOH) and $[NiFeL(\mu\text{-}O_2CMe)]BPh_4{\cdot}$MeCN (**3′**·MeCN) were selected and mounted on the tip of a polyimide loop using perfluoropolyether oil. The data set for **1**·MeOH was collected using a Stoe Stadivari diffractometer equipped with a Cu-K_α X-ray microsource (λ = 1.54178 Å) with a graded multilayer mirror monochromator and a Dectris Pilatus 300K detector. The data set for **3′**·MeCN was collected at 180(2) K using a STOE IPDS-2T image plate diffractometer system equipped with a sealed Mo X-ray tube (λ(Mo-K_α) = 0.71073 Å) and a graphite monochromator crystal. Reflection data was processed using the X-area package.[86] The structure was solved by dual-space methods[87] and refined by full-matrix least-squares techniques on the basis of all data using SHELXL-2018/3[88] and Olex2.[89] Platon was used to search for higher symmetry.[90] All non-hydrogen atoms were refined anisotropically. Graphics were produced with Diamond 4.6.8 by Crystal Impact GbR.[91] The parameter τ was calculated according to eqn (2).[55]

$$\tau = \frac{\alpha - \beta}{60^\circ} \quad (2)$$

Crystallographic data for 1·MeOH

$C_{39}H_{70}FeN_6S_2Cl_2O_9$, M_r = 957.80 g mol^{-1}, monoclinic group $P2_1/n$, a = 14.1064(3) Å, b = 17.0368(4) Å, c = 19.4289(4) Å, α = 90°, β = 92.671(2)°, γ = 90°, V = 4664.23(18) $Å^3$, Z = 4, ρ_{calcd} = 1.364 g cm^{-3}, T = 180 K, μ(Cu K_α) = 4.952 mm^{-1} (λ = 1.54186 Å), 30 056 reflections measured, 8768 unique, 7827 with $I > 2\sigma(I)$. Final R_1 = 0.0364, wR_2 = 0.0962 ($I > 2\sigma(I)$), 613 parameters/149 restraints, min./max. residual electron density = −0.34/0.47 e^- $Å^{-3}$. Due to free rotation, the ClO_4^- anions as well as the methanol solvent molecule were found to be disordered over two and three positions, respectively. These disorders were successfully modeled with a split atom model using SADI instructions implemented in SHELXL.

Crystallographic data for 3′·MeCN

$C_{66}H_{90}BFeN_7NiO_2S_2$, M_r = 1202.93 g mol^{-1}, triclinic space group $P\bar{1}$, a = 13.3261(6) Å, b = 15.6750(8) Å, c = 16.9825(7) Å, α = 108.791(4)°, β = 92.255(4)°, γ = 107.496(3)°, V = 3166.3(3) $Å^3$, Z = 2, ρ_{calcd} = 1.262 g cm^{-3}, T = 180(2) K, μ(Mo K_α) = 0.641 mm^{-1} (λ = 0.71073 Å), 22 706 reflections measured, 12 366 unique, 8827 with $I > 2\sigma(I)$. Final R_1 = 0.0428, wR_2 = 0.1003 ($I > 2\sigma(I)$), 797 parameters/24 restraints, min./max. residual electron density = 0.53/−0.57 e^- $Å^{-3}$. It has not been possible to assign the Fe and Ni atoms to the two coordination pockets. A refinement with full site occupancy factors led to R values of 0.0463 and 0.0473 for the two options. In both models the Fe and Ni bond lengths are within experimental error identical, suggesting that the metals are statistically distributed over the two coordination pockets. The refinements

were therefore carried out with 50%/50% occupancy factors using EXYZ and EADP instructions implemented in SHELX. The *t*Bu groups were found to be disordered over two positions. This disorder was successfully modelled with a split atom model using SADI instructions implemented in SHELXL.

Computational details

The calculations were done using density functional theory (DFT) within the broken symmetry approach.[92–94] The hybrid functional of Perdew, Burke and Ernzerhof (PBE0)[95,96] and Ahlrichs triple-zeta valence basis set (TZV(P))[97] as implemented in the ORCA[98,99] program package (revision 4.2.0) were used for all calculations. The geometry of all considered structures were taken from the crystal structures and were fixed during the calculations. All calculations make use of the resolution of identity (Split-RI-J) approach for the Coulomb term in combination with the chain-of-spheres approximation for the exchange term (COSX) as implemented in ORCA.[100,101] Grimme's empirical dispersion correction D3 (BJ) was employed.[102,103] All calculations were performed using increased iteration grids (GRID5 NOFINALGRID).

The calculation of J included the following steps: definition of the geometry of the molecule from X-ray analysis; calculation of the total energy for the *high-spin* (HS) state ($S = 2$); calculation of the total energy for the broken-symmetry (BS) state ($S = 0$); calculation of the J value within the following scheme:

$$J = \frac{^{BS}E(X) - {}^{HS}E(X)}{^{HS}\langle S^2\rangle - {}^{BS}\langle S^2\rangle} \quad (3)$$

where ^{HS}E, $^{HS}\langle S^2\rangle$ ^{HS}E, $^{HS}\langle S^2\rangle$ – correspond to the total energy and total spin angular momentum for the *high-spin* state (HS), ^{BS}E and $^{BS}\langle S^2\rangle$ to the total energy and total spin angular momentum for the broken-symmetry state (BS). This scheme is valid over the whole coupling strength regime.[80] For the DFT calculations required for the NCI plot,[92–94,104] the hybrid functional B3LYP[100] was used in combination with the def2-TZVP[105] basis set as implemented in ORCA 5.0.4[106–108]

Non-covalent-interaction plot analysis

NCI plots were computed with the NCIPLOT program using the electron density derived from DFT calculations.[109] For computing the NCI plots, we defined a cube with a side length of 3 Å with the midpoint between the two sulphur atoms at the cube center, in which the electron density (ρ) and the reduced density gradient (s) was computed. The representation of s *versus* sign(λ_2)ρ shows representative peaks at low density values in the presence of non-covalent interactions due to the annihilation of the reduced density gradient at these points.[110] To distinguish between attractive and repulsive interactions, the NCI approach considers the accumulation or depletion of density in the plane perpendicular to the interaction, which is mainly characterized by the second eigenvalue λ_2 of the electron-density Hessian matrix.[111]

A very important feature is the visualization of the reduced density gradient isosurfaces in real space using ChimeraX.[112] The isosurfaces at s = 0.3 a.u. are colored according to their relative strength using the value of the sign(λ_2)ρ from the generated fingerprint plot. An RGB-inspired color scale (red-green-violet) is used, where red isosurfaces represent repulsive interactions, green very weak van der Waals interactions and violet attractive interactions.

X-ray powder diffraction

PXRD measurements were carried out on a STOE STADI-P diffractometer (Stoe & Cie. GmbH, Darmstadt, Germany) equipped with a sealed Cu X-ray tube, a germanium (111) monochromator crystal (λ(Cu-K$_{\alpha1}$) = 154.060 pm) and a DECTRIS Mythen 1K detector (Baden, Switzerland). The sample was ground, filled in a glass capillary (Hilgenberg, outer diameter 0.3 mm) and measured in the Debye–Scherrer mode. Data analysis was done by STOE WinXPOW software Version 3.11. Theoretical powder diffraction from the single crystal structure (CIF file) was calculated using the WinXPOW software. The data were plotted using Origin 2019.

Scanning electron microscopy with energy-dispersive X-ray spectroscopy

SEM was performed on a leo gemini device with 20 kV acceleration voltage equipped with an Oxford Instruments 7426 EDX detector. Samples were drop coated in ^{i}PrOH to a sample holder with carbon pad and were dried at air. Samples were covered with carbon using a carbon evaporator. All images were obtained using the Everhart–Thornley detector. All EDX mappings were measured for 1 h due to the limited thickness of the crystals.

Author contributions

Vanessa Stephan: writing – original draft, visualization, validation, investigation, formal analysis. Christian Zocher: writing – review & editing, investigation, formal analysis. Martin Börner: writing – review & editing, investigation, formal analysis. Jennifer Klose: writing – review & editing. Daniel Fuhrmann: review & editing, investigation, formal analysis. Berthold Kersting: writing – review & editing, writing – original draft, supervision, resources, project administration, funding acquisition.

Conflicts of interest

There are no conflicts of interest to declare.

Data availability

All experimental data supporting the findings of this study are provided in the supplementary information (SI). Supplementary information: additional raw data, including mass spectrometry spectra, spectroscopic files, additional crys-

tallographic and DFT calculated structural data, and magnetic data. See DOI: https://doi.org/10.1039/d5dt02350e.

CCDC 2392031 (**3**) and 2392032 (**1**) contain the supplementary crystallographic data for this paper.[113a,b]

Acknowledgements

We are thankful to Prof. Dr H. Krautscheid for providing facilities for X-ray crystallographic measurements and to Prof. Dr O. Oeckler for providing facilities for SEM-EDX measurements. This project was co-financed by the European Union and tax revenues on the basis of the budget adopted by the Saxon State Parliament. This work was funded in part by the German Research Foundation (DFG) within the CRC Transregio TRR 386 – B1 (514664767). We also thank the DFG for an FTIR spectrometer (Project number 448298270). Computations for this work were done (in part) using resources of the Leipzig University Computing Center.

References

1 J. Klingele, S. Dechert and F. Meyer, *Coord. Chem. Rev.*, 2009, **253**, 2698–2741.
2 R. Robson, *Aust. J. Chem.*, 1970, **23**, 2217–2224.
3 A. L. Gavrilova and B. Bosnich, *Chem. Rev.*, 2004, **104**, 349–384.
4 B. G. Cooper, J. W. Napoline and C. M. Thomas, *Catal. Rev.*, 2012, **54**, 1–40.
5 S. Maggini, *Coord. Chem. Rev.*, 2009, **253**, 1793–1832.
6 V. Ritleng and M. J. Chetcuti, *Chem. Rev.*, 2007, **107**, 797–858.
7 R. C. Cammarota, L. J. Clouston and C. C. Lu, *Coord. Chem. Rev.*, 2017, **334**, 100–111.
8 P. Buchwalter, J. Rosé and P. Braunstein, *Chem. Rev.*, 2015, **115**, 28–126.
9 M. R. Halvagar, B. Neisen and W. B. Tolman, *Inorg. Chem.*, 2013, **52**, 793–799.
10 S. Gu, D. Xu and W. Chen, *Dalton Trans.*, 2011, **40**, 1576–1583.
11 S. Deolka, O. Rivada-Wheelaghan, S. L. Aristizábal, R. R. Fayzullin, S. Pal, K. Nozaki, E. Khaskin and J. R. Khusnutdinova, *Chem. Sci.*, 2020, **11**, 5494–5502.
12 W. Guan, S. Yamabe and S. Sakaki, *Dalton Trans.*, 2013, **42**, 8717–8728.
13 C.-F. Chow, M. H. W. Lam and W.-Y. Wong, *Anal. Chem.*, 2013, **85**, 8246–8253.
14 M. Ostrowska, I. O. Fritsky, E. Gumienna-Kontecka and A. V. Pavlishchuk, *Coord. Chem. Rev.*, 2016, **327–328**, 304–332.
15 Y. Peng and A. K. Powell, *Coord. Chem. Rev.*, 2021, **426**, 213490.
16 K. Liu, W. Shi and P. Cheng, *Coord. Chem. Rev.*, 2015, **289–290**, 74–122.
17 W. Lubitz, H. Ogata, O. Rüdiger and E. Reijerse, *Chem. Rev.*, 2014, **114**, 4081–4148.
18 Y. Ohki and K. Tatsumi, *Eur. J. Inorg. Chem.*, 2011, **2011**, 973–985.
19 J. A. Denny and M. Y. Darensbourg, *Chem. Rev.*, 2015, **115**, 5248–5273.
20 C. Pathak, S. K. Gupta, M. K. Gangwar, A. P. Prakasham and P. Ghosh, *ACS Omega*, 2017, **2**, 4737–4750.
21 C. Wombwell, C. A. Caputo and E. Reisner, *Acc. Chem. Res.*, 2015, **48**, 2858–2865.
22 (*a*) C. Tard and C. J. Pickett, *Chem. Rev.*, 2009, **109**, 2245–2274; (*b*) D. Brazzolotto, L. Wang, H. Tang, M. Gennari, N. Queyriaux, C. Philouze, S. Demeshko, F. Meyer, M. Orio, V. Artero, M. B. Hall and C. Duboc, *ACS Catal.*, 2018, **8**(11), 10658–10667; (*c*) H. Tang and M. B. Hall, *J. Am. Chem. Soc.*, 2017, **139**(49), 18065–18070; (*d*) H. Tai, Y. Higuchi and S. Hirota, *Dalton Trans.*, 2018, **47**, 4408–4423.
23 H. Ōkawa, H. Furutachi and D. E. Fenton, *Coord. Chem. Rev.*, 1998, **174**, 51–75.
24 D. E. Fenton, *Chem. Soc. Rev.*, 1999, **28**, 159–168.
25 A. J. Atkins, D. Black, A. J. Blake, A. Marin-Becerra, S. Parsons, L. Ruiz-Ramirez and M. Schröder, *Chem. Commun.*, 1996, 457–464.
26 P. Zanello, S. Tamburini, P. A. Vigato and G. A. Mazzocchin, *Coord. Chem. Rev.*, 1987, **77**, 165–273.
27 D. Huang and R. H. Holm, *J. Am. Chem. Soc.*, 2010, **132**, 4693–4701.
28 R. R. Gagne, C. L. Spiro, T. J. Smith, C. A. Hamann, W. R. Thies and A. D. Shiemke, *J. Am. Chem. Soc.*, 1981, **103**, 4073–4081.
29 R. R. Gagne and C. L. Spiro, *J. Am. Chem. Soc.*, 1980, **102**, 1443–1444.
30 M. Tadokoro, H. Ōkawa, N. Matsumoto, M. Koikawa and S. Kida, *J. Chem. Soc., Dalton Trans.*, 1991, 1657–1663.
31 A. Hori, Y. Mitsuka, M. Ohba and H. Ōkawa, *Inorg. Chim. Acta*, 2002, **337**, 113–121.
32 E. J. Larson and V. L. Pecoraro, *J. Am. Chem. Soc.*, 1991, **113**, 7809–7810.
33 J. A. Garden, P. K. Saini and C. K. Williams, *J. Am. Chem. Soc.*, 2015, **137**, 15078–15081.
34 P. K. Saini, C. Romain and C. K. Williams, *Chem. Commun.*, 2014, **50**, 4164–4167.
35 A. C. Deacy, C. B. Durr and C. K. Williams, *Dalton Trans.*, 2020, **49**, 223–231.
36 G. Trott, J. A. Garden and C. K. Williams, *Chem. Sci.*, 2019, **10**, 4618–4627.
37 K. Wang, T. J. Prior and C. Redshaw, *Chem. Commun.*, 2019, **55**, 11279–11282.
38 O. Santoro and C. Redshaw, *Catalysts*, 2020, **10**, 210.
39 P. Zanello, S. Tamburini, P. A. Vigato and G. A. Mazzocchin, *Coord. Chem. Rev.*, 1987, **77**, 165–273.
40 A. J. Atkins, D. Black, A. J. Blake, A. Marin-Becerra and S. Parsons, *Chem. Commun.*, 1996, 457–464.
41 H. Ōkawa, H. Furutachi and D. E. Fenton, *Coord. Chem. Rev.*, 1998, **174**, 51–75.
42 M. Tadokoro, H. Ōkawa, N. Matsumoto, M. Koikawa and S. Kida, *J. Chem. Soc., Dalton Trans.*, 1991, 1657–1663.

43 J. Nishio, H. Ōkawa, S. Ohtsuka and M. Tomono, *Inorg. Chim. Acta*, 1994, **218**, 27–32.
44 D. Huang and R. H. Holm, *J. Am. Chem. Soc.*, 2010, **132**, 4693–4701.
45 S. Mohanta, S. Baitalik, S. K. Dutta and B. Adhikary, *Polyhedron*, 1998, **17**, 2669–2677.
46 B. Kersting and G. Steinfeld, *Chem. Commun.*, 2001, 1376–1377.
47 (*a*) Y. Journaux, V. Lozan, J. Klingele and B. Kersting, *Chem. Commun.*, 2006, 83–84; (*b*) S. Brooker, *Coord. Chem. Rev.*, 2001, **222**(1), 33–56; (*c*) A. Christensen, C. Mayer, F. Jensen, A. D. Bond and C. J. McKenzie, *Dalton Trans.*, 2006, 108–120.
48 M. Börner, D. Fuhrmann, J. Klose, H. Krautscheid and B. Kersting, *Inorg. Chem.*, 2021, **60**, 13517–13527.
49 G. Steinfeld and B. Kersting, *Chem. Commun.*, 2000, 205–206.
50 C. Núñez, R. Bastida, A. Macías, L. Valencia, J. Ribas, J. L. Capelo and C. Lodeiro, *Dalton Trans.*, 2010, **39**, 7673–7683.
51 M. Gressenbuch and B. Kersting, *Z. Anorg. Allg. Chem.*, 2016, **642**, 719–723.
52 V. Lozan, C. Loose, J. Kortus and B. Kersting, *Coord. Chem. Rev.*, 2009, **253**, 2244–2260.
53 T. Fritz, G. Steinfeld, S. Käss and B. Kersting, *Dalton Trans.*, 2006, 3812–3821.
54 Y. Journaux, T. Glaser, G. Steinfeld, V. Lozan and B. Kersting, *Dalton Trans.*, 2006, 1738–1748.
55 A. W. Addison, T. Nageswara Rao, J. Reedijk, J. van Rijn and G. C. Verschoor, *J. Chem. Soc., Dalton Trans.*, 1984, 1349–1356.
56 S. C. Shoner, A. M. Nienstedt, J. J. Ellison, I. Y. Kung, D. Barnhart and J. A. Kovacs, *Inorg. Chem.*, 1998, **37**, 5721–5726.
57 T. Komuro, T. Matsuo, H. Kawaguchi and K. Tatsumi, *Inorg. Chem.*, 2003, **42**, 5340–5347.
58 C.-Y. Chiang, M. L. Miller, J. H. Reibenspies and M. Y. Darensbourg, *J. Am. Chem. Soc.*, 2004, **126**, 10867–10874.
59 M. Mantina, A. C. Chamberlin, R. Valero, C. J. Cramer and D. G. Truhlar, *J. Phys. Chem. A*, 2009, **113**, 5806–5812.
60 E. M. Gale, B. S. Narendrapurapu, A. C. Simmonett, H. F. I. Schaefer and T. C. Harrop, *Inorg. Chem.*, 2010, **49**, 7080–7096.
61 S. J. Grabowski, *Understanding Hydrogen Bonds*, The Royal Society Of Chemistry, 2020.
62 L. A. H. van Bergen, M. Alonso, A. Palló, L. Nilsson, F. De Proft and J. Messens, *Sci. Rep.*, 2016, **6**, 30369.
63 J. Contreras-García, E. R. Johnson, S. Keinan, R. Chaudret, J.-P. Piquemal, D. N. Beratan and W. Yang, *J. Chem. Theory Comput.*, 2011, **7**, 625–632.
64 E. R. Johnson, S. Keinan, P. Mori-Sánchez, J. Contreras-García, A. J. Cohen and W. Yang, *J. Am. Chem. Soc.*, 2010, **132**, 6498–6506.
65 L. A. H. van Bergen, M. Alonso, A. Palló, L. Nilsson, F. De Proft and J. Messens, *Sci. Rep.*, 2016, **6**, 30369.
66 J. R. Lane, J. Contreras-García, J.-P. Piquemal, B. J. Miller and H. G. Kjaergaard, *J. Chem. Theory Comput.*, 2013, **9**, 3263–3266.
67 J. Contreras-García, W. Yang and E. R. Johnson, *J. Phys. Chem. A*, 2011, **115**, 12983–12990.
68 R. D. Shannon and C. T. Prewitt, *Acta Crystallogr., Sect. B*, 1969, **25**, 925–946.
69 R. D. Shannon, *Acta Crystallogr., Sect. A*, 1976, **32**, 751–767.
70 S. A. Cantalupo, H. E. Ferreira, E. Bataineh, A. J. King, M. V. Petersen, T. Wojtasiewicz, A. G. DiPasquale, A. L. Rheingold and L. H. Doerrer, *Inorg. Chem.*, 2011, **50**, 6584–6596.
71 D. H. Busch, P. H. Merrell, V. L. Goedken and J. A. Stone, *J. Am. Chem. Soc.*, 1970, **92**, 7590–7591.
72 C. Hu, B. C. Noll, C. E. Schulz and W. R. Scheidt, *Inorg. Chem.*, 2010, **49**, 10984–10991.
73 M. Ciampolini and G. P. Speroni, *Inorg. Chem.*, 1966, **5**, 45–49.
74 M. Ciampolini and N. Nardi, *Inorg. Chem.*, 1966, **5**, 41–44.
75 F. A. Cotton and M. D. Meyers, *J. Am. Chem. Soc.*, 1960, **82**, 5023–5026.
76 B. Kersting, *Angew. Chem., Int. Ed.*, 2001, **40**, 3987–3990.
77 J. Hausmann, S. Käss, S. Klod, E. Kleinpeter and B. Kersting, *Eur. J. Inorg. Chem.*, 2004, **2004**, 4402–4411.
78 X. Zhu, X.-Y. Wang, B.-L. Li, J. Wang and S. Gao, *Polyhedron*, 2012, **31**, 77–81.
79 O. K. Medhi, S. Mazumdar and S. Mitra, *Inorg. Chem.*, 1989, **28**, 3243–3248.
80 T. Soda, Y. Kitagawa, T. Onishi, Y. Takano, Y. Shigeta, H. Nagao, Y. Yoshioka and K. Yamaguchi, *Chem. Phys. Lett.*, 2000, **319**, 223–230.
81 (*a*) O. Kahn, *Molecular Magnetism*, VCH Publishers, New York NY, 1993; (*b*) D. A. Pantazis, *J. Chem. Theory Comput.*, 2019, **15**, 938–948; (*c*) D. E. Bolster, P. Gütlich, W. E. Hatfield, S. Kremer, E. W. Müller and K. Wieghardt, *Inorg. Chem.*, 1983, **22**, 1725–1729.
82 T. Glaser, F. Kesting, T. Beissel, E. Bill, T. Weyhermüller, W. Meyer-Klaucke and K. Wieghardt, *Inorg. Chem.*, 1999, **38**, 722–732.
83 T. Glaser, T. Beissel, E. Bill, T. Weyhermüller, V. Schünemann, W. Meyer-Klaucke, A. X. Trautwein and K. Wieghardt, *J. Am. Chem. Soc.*, 1999, **121**, 2193–2208.
84 R. T. Azuah, L. R. Kneller, Y. Qiu, P. L. W. Tregenna-Piggott, C. M. Brown, J. R. D. Copley and R. M. Dimeo, *J. Res. Natl. Inst. Stand. Technol.*, 2009, **114**, 341–358.
85 N. G. Connelly and W. E. Geiger, *Chem. Rev.*, 1996, **96**, 877–910.
86 Stoe & Cie, X-AREA and X-RED 32; V1.35, Stoe & Cie: Darmstadt, 2006.
87 G. M. Sheldrick, Crystal Structure Refinement with SHELXL, *Acta Crystallogr.*, 2015, **C71**, 3–8.
88 G. M. Sheldrick, SHELXT Integrated Space-Group and Crystal Structure Determination, *Acta Crystallogr.*, 2015, **C71**, 3–8.
89 O. V. Dolomanov, L. J. Bourhis, R. J. Gildea, J. A. Howard and K. H. Puschmann, OLEX2: A Complete Structure

Solution, Refinement and Analysis Program, *J. Appl. Crystallogr.*, 2009, **42**, 339–341.
90 A. L. Spek, *PLATON - A Multipurpose Crystallographic Tool; Utrecht University*, Utrecht, The Netherlands, 2000.
91 K. Brandenburg, *Diamond, Crystal Impact GbR*, Bonn, Germany, 1999.
92 L. Noodleman, C. Y. Peng, D. A. Case and J.-M. Mouesca, *Coord. Chem. Rev.*, 1995, **144**, 199–244.
93 L. Noodleman and E. R. Davidson, *Chem. Phys.*, 1986, **109**, 131–143.
94 L. Noodleman, *J. Chem. Phys.*, 1981, **74**, 5737–5743.
95 C. Adamo and V. Barone, *J. Chem. Phys.*, 1999, **110**, 6158–6170.
96 J. P. Perdew, K. Burke and M. Ernzerhof, *Phys. Rev. Lett.*, 1996, **77**, 3865–3868.
97 A. Schäfer, H. Horn and R. Ahlrichs, *J. Chem. Phys.*, 1992, **97**, 2571–2577.
98 F. Neese, *Int. J. Quantum Chem.*, 2001, **83**, 104–114.
99 F. Neese, *J. Chem. Phys.*, 2003, **119**, 9428–9443.
100 F. Neese, F. Wennmohs, A. Hansen and U. Becker, *Chem. Phys.*, 2009, **356**, 98–109.
101 R. Izsák and F. Neese, *J. Chem. Phys.*, 2011, **135**, 144105.
102 S. Grimme, J. Antony, S. Ehrlich and H. Krieg, *J. Chem. Phys.*, 2010, **132**, 154104.
103 S. Grimme, S. Ehrlich and L. Goerigk, *J. Comput. Chem.*, 2011, **32**, 1456–1465.
104 F. Neese, *Chem. Phys. Lett.*, 2000, **325**, 93–98.
105 D. Bykov, T. Petrenko, R. Izsák, S. Kossmann, U. Becker, E. Valeev and F. Neese, *Mol. Phys.*, 2015, **113**, 1961–1977.
106 "Software update: The ORCA program system—Version 5.0 - Neese - 2022 - WIREs Computational Molecular Science - Wiley Online Library", can be found under https://wires.onlinelibrary.wiley.com/doi/10.1002/wcms.1606.
107 F. Neese, *J. Comput. Chem.*, 2023, **44**, 381–396.
108 G. L. Stoychev, A. A. Auer and F. Neese, *J. Chem. Theory Comput.*, 2017, **13**, 554–562.
109 J. Contreras-García, E. R. Johnson, S. Keinan, R. Chaudret, J.-P. Piquemal, D. N. Beratan and W. Yang, *J. Chem. Theory Comput.*, 2011, **7**, 625–632.
110 R. A. Boto, J. Contreras-García, J. Tierny and J.-P. Piquemal, *Mol. Phys.*, 2016, **114**, 1406–1414.
111 J. Contreras-García, E. R. Johnson, S. Keinan, R. Chaudret, J.-P. Piquemal, D. N. Beratan and W. Yang, *J. Chem. Theory Comput.*, 2011, **7**, 625–632.
112 E. F. Pettersen, T. D. Goddard, C. C. Huang, G. S. Couch, D. M. Greenblatt, E. C. Meng and T. E. Ferrin, *J. Comput. Chem.*, 2004, **25**, 1605–1612.
113 (*a*) CCDC 2392031: Experimental Crystal Structure Determination, 2025, DOI: 10.5517/ccdc.csd.cc2l939b; (*b*) CCDC 2392032: Experimental Crystal Structure Determination, 2025, DOI: 10.5517/ccdc.csd.cc2l93bc.